

## Apparent Fracture in Polymeric Fluids Under Step Shear

Okpeafoh S. Agimelen and Peter D. Olmsted\*

*Soft Matter Physics Group, School of Physics and Astronomy, University of Leeds, Leeds LS2 9JT, United Kingdom*

(Received 18 April 2012; published 16 May 2013)

Recent step strain experiments in well-entangled polymeric liquids demonstrated a bulk fracturelike phenomenon. We study this instability by using a modern version of the Doi-Edwards theory for entangled polymers, and we find close quantitative agreement with the experiments. The phenomenon occurs because the viscoelastic liquid is sheared into a rubbery state that possesses an elastic constitutive instability [G. Marrucci and N. Grizzuti, *J. Rheol.* **27**, 433 (1983)]. The fracture is a transient manifestation of this instability, which relies on the amplification of spatially inhomogeneous fluctuations. This mechanism differs from the fracture in glassy materials and dense suspensions.

DOI: [10.1103/PhysRevLett.110.204503](https://doi.org/10.1103/PhysRevLett.110.204503)

PACS numbers: 47.50.Cd, 47.20.Gv, 47.50.Gj, 83.60.Wc

*Introduction.*—Viscoelastic liquids have slow time scales due to the relaxation of internal degrees of freedom such as polymer deformation or the structures of self-assembled materials such as amphiphiles. These slow time scales give rise to dramatic effects, such as rubbery behavior at high deformation rates, viscous behavior at lower rates, and *both* solidlike and liquidlike features. Materials such as amorphous solid polymers [1] or metallic glasses [2] have arguably the most dramatic behavior possible for a solid: rupture, fracture, and flow at a macroscopically sharp interface. This has been modeled as collective rupture of shear transformation zones [3] and in dense colloidal materials as due to the coupling between shear and density [4].

Recent experiments have demonstrated fracturelike behavior in well-entangled polymeric *liquids*. Very rapid step strains were applied to polymer melts [e.g., poly(styrene-butadiene) [5] or poly(ethylene oxide) [6]] with  $Z \approx 53$ –160 entanglements per polymer. At such high shear rates, the liquid becomes rubbery and solidlike. After the step strain the solidlike melt relaxes homogeneously for a short time, followed by a rapid relaxation during which the material splits into two layers moving in opposite directions, separated by a thin ( $\approx 40 \mu\text{m}$ ) shear band or “fracture” layer [Fig. 1 of Ref. [5]]. Reference [5] suggested that this is due to microscopic yield, such as a sudden localized chain pullout or loss of entanglements, perhaps analogous to the shear transformation zone picture for yield in amorphous solids [4].

We show that these results can be explained by a pure constitutive instability due to the effects of shear flow on the elastic stress in the fluid, and it is actually contained in the Doi-Edwards (DE) theory of entangled polymers [7–9]; this provides yet another mechanism for fracture, due purely to a constitutive shear instability in a viscoelastic liquid brought suddenly into a (transient) solid state.

The motion of an entangled polymer is restricted to a tubelike region due to the constraints imposed by surrounding chains. The DE theory for this [7] predicts a maximum in the shear stress  $T_{xy}$  as a function of shear rate [Fig. 1(a)],

at a shear rate  $\dot{\gamma}$  roughly equal to the reciprocal of the time  $\tau_d$  for a polymer to diffuse (or reptate) along its tube. This nonmonotonic constitutive behavior (which was not inferred in early experiments on polymer melts [10]) indicates instability, which can lead to inhomogeneous flows and *shear banding* [11]. This constitutive instability was widely implicated [12] in the spurt effect [13], responsible for instabilities in industrial processes; however, spurt is now usually attributed to wall slip [14]. In rapid startup flow, the DE theory predicts the rubbery behavior of a stress overshoot [7–9]. Modern theories incorporate chain stretch and convected constraint release—chain relaxation due to the release of entanglement constraints, which restores stable constitutive behavior [15]. However, new observations of shear banding seem to validate the DE instability [9,16,17] in some cases. We will show that apparent fracture is another manifestation of the DE instability.

*Model.*—We separate the total stress tensor  $\mathbf{T}$  into contributions from the polymer and a Newtonian solvent, as  $\mathbf{T} = G\mathbf{W} + \eta(\boldsymbol{\kappa} + \boldsymbol{\kappa}^T) - p\mathbf{I}$ , where  $G$  is a modulus,  $\eta$  is the solvent viscosity, the pressure  $p$  maintains incompressibility,  $\mathbf{I}$  is the identity tensor, and  $\kappa_{\alpha\beta} = \nabla_{\beta}v_{\alpha}$ . The fluid velocity  $\mathbf{v}$  (with no slip boundary conditions) with mass density  $\rho$  obeys

$$\rho \frac{d\mathbf{v}}{dt} \equiv \rho \left[ \frac{\partial}{\partial t} + (\mathbf{v} \cdot \nabla) \right] \mathbf{v} = \nabla \cdot \mathbf{T}, \quad (1)$$

where  $\nabla \cdot \mathbf{T} = 0$  for very small Reynolds numbers, as is the case here. The dimensionless polymeric conformation, or strain, tensor  $\mathbf{W}$  is assumed to obey the diffusive Rolie-Poly model [9,18]:

$$\begin{aligned} \frac{d\mathbf{W}}{dt} = & \boldsymbol{\kappa} \cdot \mathbf{W} + \mathbf{W} \cdot \boldsymbol{\kappa}^T - \frac{1}{\tau_d}(\mathbf{W} - \mathbf{I}) - \frac{2\left(1 - \sqrt{\frac{3}{\text{Tr}\mathbf{W}}}\right)}{\tau_R} \\ & \times \left( \mathbf{W} + \beta \sqrt{\frac{3}{\text{Tr}\mathbf{W}}}(\mathbf{W} - \mathbf{I}) \right) + \mathcal{D}\nabla^2\mathbf{W}, \end{aligned} \quad (2)$$

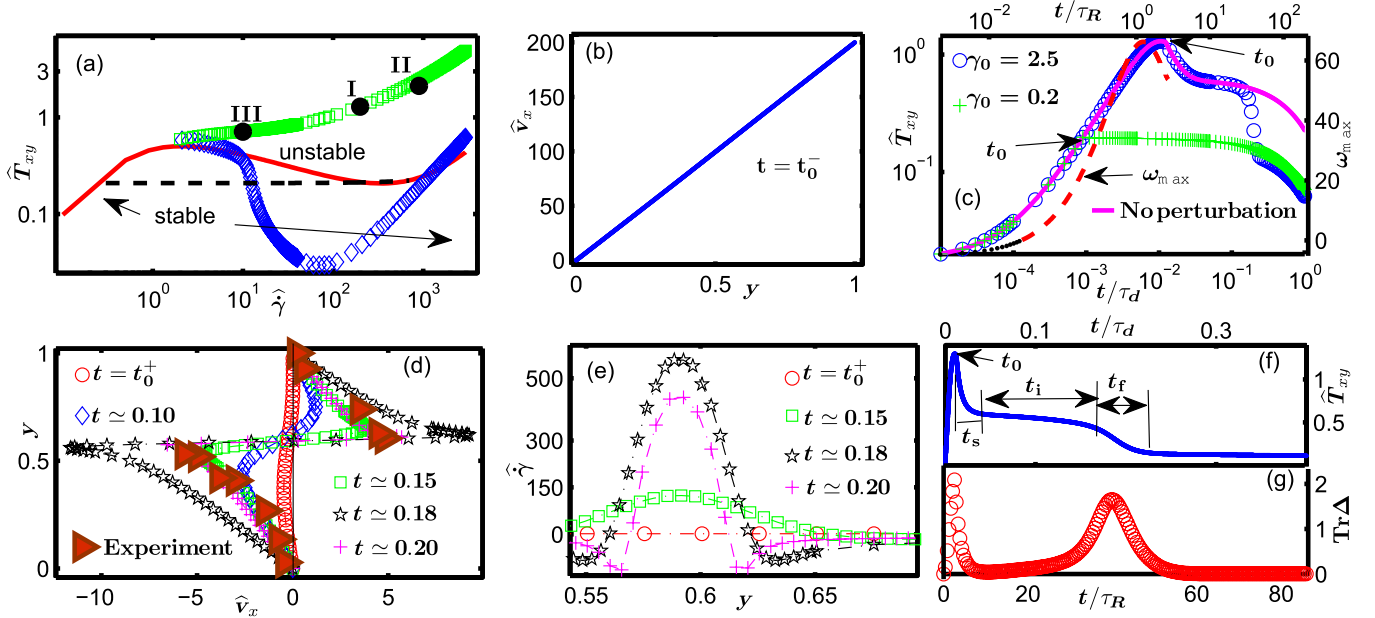


FIG. 1 (color online). (a) Constitutive (solid line) and steady state shear banding (black dashes) curves. The stress overshoot is indicated by green squares; small perturbations grow exponentially in time ( $\omega_{max} > 0$ ) for stresses exceeding the stress given by the blue diamonds. The stresses at  $t_0$  for three cases described in the text are indicated by I, II, and III. (b) Velocity profile at  $t_0^-$  (just before shear cessation) for  $\langle \hat{\gamma} \rangle = 200$ . (c) Stress relaxation for step strains  $\gamma_0 = 0.2, 2.5$ ; the solid line is for  $\gamma_0 = 2.5$  with no initial perturbation. The dot-dashed line shows the evolution of the most unstable eigenvalue  $\omega_{max}$ , which becomes unstable ( $\omega_{max} > 0$ ) in the red (dashed) region. (d) Velocity profiles during fracture, with experimental data from [5] superposed. (e) Shear rate profiles, (f) stress relaxation, and (g) evolution of the maximum stretch in the gap  $\text{Tr} \Delta^{max}$ . [Parameters:  $Z = 72$ ,  $\tau_R = \tau_d/216$ ,  $\langle \hat{\gamma} \rangle = 200$ ,  $\gamma_0 = 2.5$ ,  $t_0 = 0.01250\tau_d$ , and  $t_0^\pm = t_0 \pm 10^{-5}\tau_d$ . Times  $t$  and  $1/\omega_{max}$  are displayed in units of  $\tau_d$ .]

which is a simplified form of the Graham-Likhtman-Milner-McLeish (GLaMM) model, itself a modern version of Doi-Edwards theory [19]. Here,  $\tau_d$  is the reptation time, and the Rouse time  $\tau_R$  governs the relaxation of stretch  $\text{Tr}(\mathbf{W})$ . The parameter  $\beta$  quantifies convected constraint release; a large value of  $\beta$  corresponds to more convected constraint release, which leads to monotonic (stable) behavior of the shear stress. Spatial gradients due to stress “diffusivity”  $\mathcal{D}$  are subject to the boundary condition  $\nabla \mathbf{W} = 0$  [11].

*Calculations.*—We consider two infinite flat plates separated by  $L\hat{y}$  where the top plate moves parallel to  $\hat{x}$  and the bottom plate is fixed. The velocity field is thus given by  $\mathbf{v} = v_x(t, y)\hat{x}$ , and  $\mathbf{W} \equiv \mathbf{W}(t, y)$ . We define dimensionless quantities  $\hat{\gamma} = \gamma\tau_d$ ,  $\hat{\mathcal{D}} = \mathcal{D}\tau_d/L^2$ ,  $\epsilon = \eta/(G\tau_d)$ ,  $\hat{\rho} = \rho L^2/(G\tau_d^2)$ ,  $\hat{v} = \tau_d v/L$ , and  $\hat{t} = t/\tau_d$ . The degree of entanglement  $Z$  determines the Rouse time via  $\tau_R = \tau_d/(3Z)$  [18,19]. A desired average shear rate is imposed for a duration  $t_0$  leading to a strain  $\gamma_0 = \langle \hat{\gamma} \rangle t_0$ .

The values  $\tau_d = 310$  s and  $Z = 55$ – $100$  are consistent with the data in [5]; with  $\eta \approx 1$  Pa s and  $G \approx 7 \times 10^3$  Pa [20] we find  $\epsilon \approx 10^{-7}$ ; for numerical stability, we use  $\epsilon = 10^{-4}$ . For  $L = 1$  mm,  $\rho \approx 10^3$  kg m $^{-3}$  gives  $\hat{\rho} \approx 10^{-10}$ , and we use  $\hat{\mathcal{D}} = 10^{-5}$  [21]. Spatial derivatives are discretized by using a semi-implicit central finite difference scheme. For a time step  $\delta\hat{t} = 10^{-6}$  and 1000 spatial mesh points, the maximum velocity in the fracture and time to fracture converge within a few percent.

We infer (in)stability by considering the evolution of perturbations to the uniform solution to Eq. (2):  $\mathbf{s}(t) \equiv [\Delta_{xx}, \Delta_{xy}, \Delta_{yy}](t)$ , where  $\Delta = \mathbf{W} - \mathbf{I}$ , with initial conditions  $\mathbf{s}(0) = [0, 0, 0]$  and imposed uniform shear rate  $\hat{\gamma}$ . At some time  $t_0$  we impose an inhomogeneous perturbation  $\delta\mathbf{u}(y, t_0) = [\delta\hat{\gamma}, \delta\Delta_{xx}, \delta\Delta_{xy}, \delta\Delta_{yy}](y, t_0) = \sum_k \delta\mathbf{u}_k(t_0) \exp(iky)$ . The full dynamics is thus given by  $\mathbf{u}(y, t; t_0) = [\hat{\gamma}, \mathbf{s}](t_0) + \delta\mathbf{u}(y, t - t_0)$ . The perturbation  $\delta\mathbf{u}$  evolves for small times  $t - t_0$  according to the dynamics given by linearizing Eqs. (1) and (2):  $\delta\dot{\mathbf{u}}_k(t - t_0) = \mathbf{M}_k[\mathbf{s}(t_0)]\delta\mathbf{u}_k(t - t_0)$ . The growth or decay of this perturbation at early times indicates whether the perturbation can induce fracture after shearing is stopped at  $t_0$ . The perturbation will grow after  $t_0$  when the largest real part  $\omega_{max}$  of the spectrum of eigenvalues of  $\mathbf{M}_k$  is positive.

To capture the behavior reported in [5], we consider a fluid with nonmonotonic constitutive behavior,  $\beta = 0$  [solid line in Fig. 1(a)], and use  $Z = 72$  (consistent with [5]); this leads to shear banding and a stress plateau in the steady state [dashes in Fig. 1(a)] [11]. We initialize Eq. (2) with random perturbations  $\delta\mathbf{u}(0, y) = \xi \sum_{n=1}^5 (\mathbf{A}_n/n^2) \times \cos n\pi y$ ,  $A_{ni} \in [-1, 1]$ , where  $i$  are the four components of  $\mathbf{A}_n$ ; here,  $\xi$  sets the scale of the perturbation. The penalty  $1/n^2$  arises because high wave numbers  $n$  should be suppressed by both spatial gradients in  $\mathbf{W}$  and by the slow dynamics of long wavelength velocity fluctuations that induce perturbations upon sample loading (for

example). We use  $\xi = 0.01$ , consistent with the scale of typical thermal fluctuations in  $\mathbf{W}$  [22].

Perturbations can grow if the fluid becomes unstable [8,22–24]. For 34% of 300 sets of randomly chosen  $\mathbf{A}_n$ , the resulting velocity profiles were similar to those reported in [5]. Using initial conditions that produce the experimentally observed velocity profile, we simulate examples reported in [5]. The green squares in Fig. 1(a) are the overshoot stresses at different shear rates, and the stresses at  $t_0$  for the three cases studied are indicated as I, II, and III. For times  $t_0$  later than the time at which the startup stress is given by the blue diamonds, the perturbation  $\delta\mathbf{u}$  grows exponentially upon shear cessation. This is where we infer instability.

*Case I.*—For  $\langle\dot{\gamma}\rangle\tau_R \approx 1$  and  $\gamma_0 > \gamma_{ov}$  (the overshoot strain), we impose  $\langle\hat{\gamma}\rangle = 200$  ( $\langle\dot{\gamma}\rangle\tau_R = 0.93$ ) for  $\gamma_0 = 2.5$ . Immediately before cessation at  $t_0^-$ , the velocity profile is imperceptibly inhomogeneous [Fig. 1(b)], while at  $t_0^+$  the fluid has stopped with a slight inhomogeneity induced by the perturbation [Fig. 1(d)]. Some stress then quickly relaxes due to stretch relaxation in a time  $t_s \approx 7\tau_R$  [Figs. 1(c), 1(f), and 1(g)], followed by an induction time  $t_i \approx 30\tau_R$  with relaxation due to reptation [blue circles in Figs. 1(c) and 1(f)]. The perturbation slowly grows during  $t_i$  and localizes, leading to a fracture plane at which the fluid shears very rapidly [Figs. 1(d) and 1(e)], and a sizable stretch  $\text{Tr}\Delta$  is induced [Fig. 1(g)]. The stress relaxes quickly during this localization in a time  $t_f \approx 15\tau_R$  [Figs. 1(c) and 1(f)]. Thereafter it relaxes like a quiescent melt with a small initial strain  $\gamma_0 = 0.2$  [Fig. 1(c)]. Since the boundaries are fixed, positive shear strain within the slip layer is balanced by opposing recoil in the still-entangled outer regions [e.g., Fig. 1(e) for  $t/\tau_d > 0.15$ ]. Without an initial perturbation, only quiescent relaxation is obtained [solid line in Fig. 1(c)]. The velocity profiles [Fig. 1(d)] are consistent with Fig. 1 of Ref. [5] (which has an induction time  $t_i \approx 5\tau_R$ ).

*Stability.*—Figures 1(a) and 1(c) suggest that the material is unstable ( $\omega_{\max} > 0$ ) from well before the stress overshoot until shear cessation. To understand this instability, we turn to the Marrucci-Grizzuti observation that for strain  $\gamma_0 \gtrsim 2.1$  the elastic energy function  $F(\gamma)$  for the DE model has a negative effective shear modulus  $\mathcal{A} \equiv \partial^2 F / \partial \gamma^2 < 0$  [8], which heralds instability. Marrucci and Grizzuti predicted elastic instability for a step strain, for

$$\mathcal{A}^{\text{eff}} \equiv \mu(t_0 + t_s) \left. \frac{\partial^2 F}{\partial \gamma^2} \right|_{\gamma_0} + [1 - \mu(t_0 + t_s)] \left. \frac{\partial^2 F}{\partial \gamma^2} \right|_0 < 0, \quad (3)$$

where  $\mu(t)$  is the fraction of unrelaxed material. The elastic limit  $\dot{\gamma}\tau_d \gg 1$  gives  $\mathcal{A}^{\text{eff}} \approx \partial T_{xy} / \partial \gamma = \dot{\gamma}^{-1} \partial T_{xy} / \partial t < 0$  [8,17,22,23], which coincides with the stress overshoot.

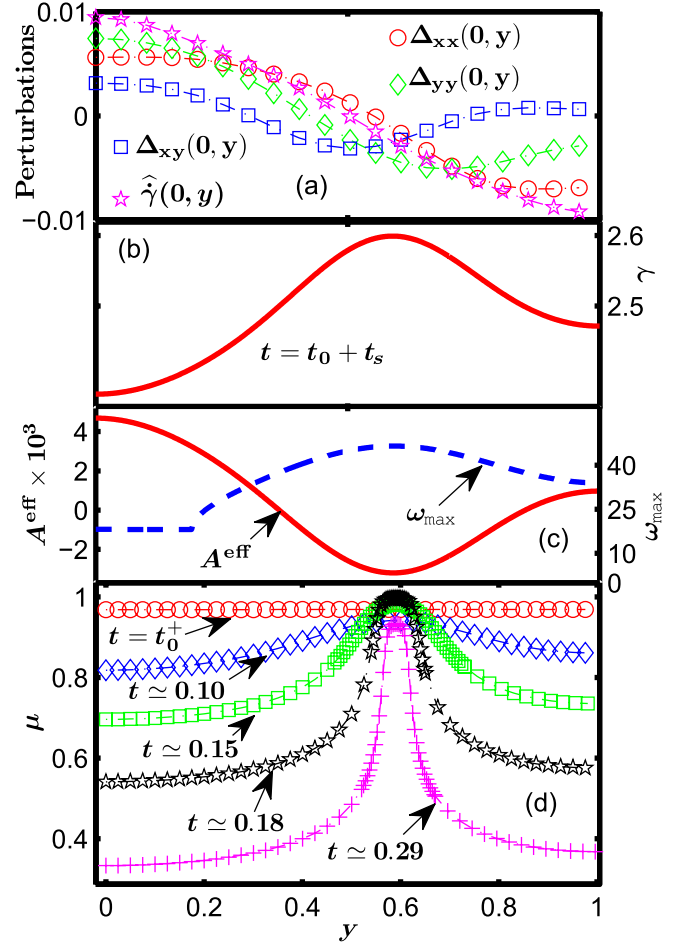


FIG. 2 (color online). Spatial profiles of (a) initial perturbation, (b) local strain, and (c) effective modulus  $\mathcal{A}^{\text{eff}}$  as well as the unstable growth rate  $\omega_{\max}$ , after cessation of flow and subsequent stretch relaxation. (d) Evolution of unrelaxed polymer segments  $\mu(y, t)$  during fracture development. [Parameters are as in Fig. 1. Time  $t$  is displayed in units of  $\tau_d$ .]

The anisotropy of the polymer conformation tensor  $\mathbf{W}$  defines  $\mu = |\lambda_1 - \lambda_2| / |\lambda_1 + \lambda_2|$ , where  $\lambda_i$  are the eigenvalues of  $\mathbf{W}$  in the plane containing the velocity gradient and flow directions [25]. For a homogeneous initial condition,  $\mu(t)$  relaxes homogeneously to zero, while an inhomogeneous initial condition initiates instability and an inhomogeneous  $\mu(y, t)$  [Fig. 2(d)].

Figures 2(d) and 2(c) show the spatial profiles for the strain and the effective shear modulus  $\mathcal{A}^{\text{eff}}$  after stretch relaxation [26]. The fracture region is most unstable, so that the initial perturbation [Fig. 2(a)] can localize strain. The unstable region predicted by the elastic limit coincides with the most unstable eigenvalue  $\omega_{\max}$  calculated from the full dynamics, which indicates instability before the stress overshoot is reached [e.g., Fig. 1(a)] because of the viscous contribution to the instability [23]. The most unstable eigenvector is dominated by the growth of  $\Delta_{xx}$  [24], which enhances stretch in the flow direction.

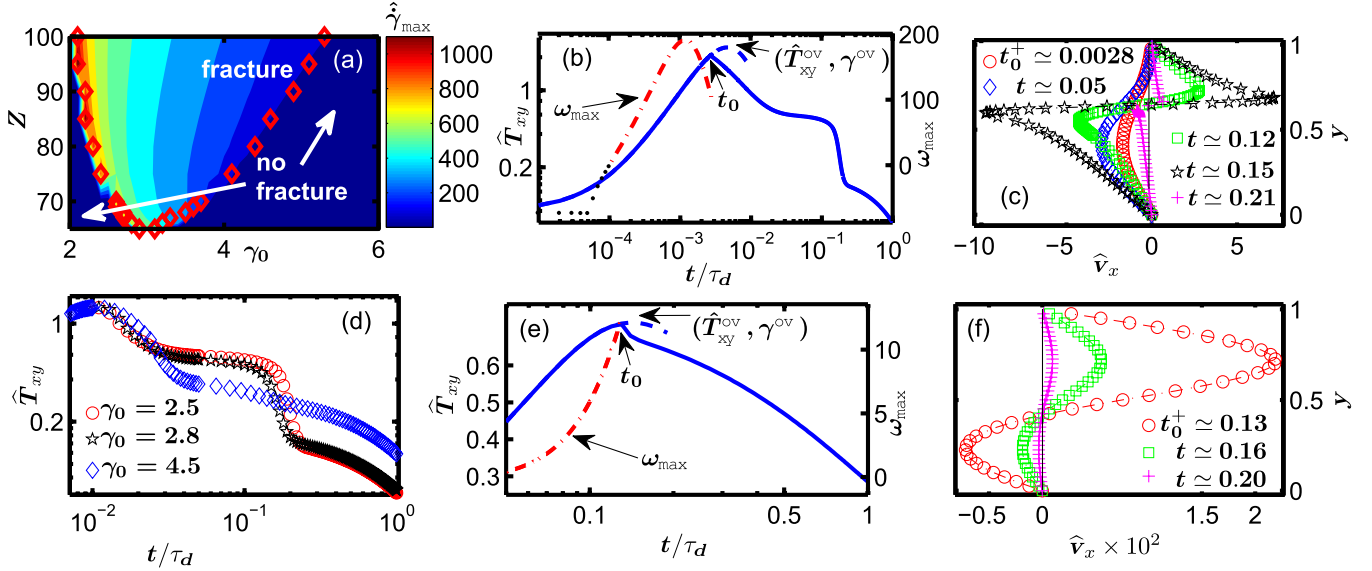


FIG. 3 (color online). (a) Values of  $Z$  and  $\gamma_0$  required for fracture at fixed  $\langle \hat{\gamma} \rangle$ ; contours show the maximum local shear rates during fracture. (b), (c) Case II ( $\langle \hat{\gamma} \rangle = 900$ ,  $\langle \dot{\gamma} \rangle \tau_R = 4.2$ ,  $\gamma_0 = 2.5$ ): (b) stress relaxation and unstable growth rate  $\omega_{\max}$  (the dashed line is the stress overshoot with no initial perturbation); (c) velocity profiles during fracture. (d) Stress decay for three different imposed strains  $\gamma_0$ . (e), (f) Case III ( $\langle \hat{\gamma} \rangle = 10$ ,  $\langle \dot{\gamma} \rangle \tau_R = 0.046$ ,  $\gamma_0 = 1.3$ ): (e) stress relaxation and  $\omega_{\max}$  and (f) velocity profiles. [All other parameters are as in Fig. 1. Time  $t$  is displayed in units of  $\tau_d$ .]

*Conditions for fracture.*—A detailed study shows that perturbations in  $\Delta_{xx}$  and  $\Delta_{yy}$  induce fracture [24]. The step strain  $\gamma_0$  advects the initial perturbation into a shear component of the polymer strain (e.g.,  $W_{xy}(y, t_0) \approx \gamma_0[1 + \Delta_{yy}(y, 0)]$ ), which generates an inhomogeneous shear rate  $\delta \hat{\gamma}(y, t_0^+) \approx -\gamma_0 \Delta_{yy}(y, 0)/\epsilon$  immediately after cessation of flow to maintain  $\nabla \cdot \mathbf{T} \approx 0$ . Although general perturbations are complex [Fig. 2(a)] [24], a local maximum in the *polymeric strain*  $\gamma$  defines the position with the most negative effective shear modulus  $\mathcal{A}_{\text{eff}} < 0$  and the fastest growth rate  $\omega_{\max}$  [Fig. 2(c)] [26] and, thus, the fracture position.

The subsequent evolution resembles spinodal decomposition of a conserved quantity, since the total strain  $\gamma_0$  is fixed. The strain in the most unstable region grows, while that in the less unstable regions decreases. This leads to recoil and a sharpening of the deformation around the most unstable position, which can then fracture if the initial amplitude grows quickly enough compared to the overall relaxation due to reptation. Significant convected constraint release suppresses fracture because of the enhanced relaxation.

*Character of fracture.*—A larger strain leads to a less dramatic fracture [Figs. 3(a) and 3(d)], because the total stress has passed the overshoot and decreased, hence releasing less stress into the fracture; however, the larger molecular strain  $W_{xy}$  leads to a faster growing instability, which is consistent with Fig. 8 of Ref. [5]. Alternatively, for a higher imposed strain rate and  $t_0$  beyond the overshoot, the stretch-dominated response leaves less orientational stress and molecular strain after stretch relaxation, so that fracture takes longer to develop [23].

In case II ( $\langle \hat{\gamma} \rangle = 900$ ,  $\langle \dot{\gamma} \rangle \tau_R = 4.2$ ), the shear rate is large but the strain  $\gamma_0 = 2.5$  is slightly less than the overshoot strain  $\gamma_{\text{ov}}$  [Figs. 3(b) and 3(c)]. The velocity profiles are consistent with Fig. 2 of Ref. [5]. Because the growth rate  $\omega_{\max}$  is so rapid for the high shear rate, the smaller strain can effect the necessary large growth of the instability. In this case, the induction time and velocity profiles are similar to case I. In case III ( $\langle \hat{\gamma} \rangle = 10$ ,  $\langle \dot{\gamma} \rangle \tau_R = 0.046$ ) the shear rate is relatively small [Figs. 3(e) and 3(f)], and fracture and recoil are very weak due to the small growth rate. The stress response due to the inhomogeneity is almost negligible compared to that of an unperturbed initial condition. The weak recoil agrees with Fig. 7 of Ref. [5].

Figure 6 of Ref. [5] demonstrated that, for subovershoot strains, higher shear rates lead to longer induction times, while our calculations predict shorter induction times because of the faster growing instability [24]. We cannot explain this discrepancy.

*Conclusion.*—We have shown that the fracture seen in recent step strain experiments on polymeric liquids [5,6] could result from an underlying elastic instability in the DE model, whose signature is stress overshoot during rapid startup [8,9,27]. Once stretch degrees of freedom have relaxed, the deformed melt is elastically unstable so that small inhomogeneities grow into plastic strain (shear flow) in the most unstable regions. If this instability grows fast enough compared to reptation, then a dramatic fracture can result. The perturbation's shape and amplitude control whether fracture occurs.

In related works, Manning *et al.* studied a shear-transformation-zone model of an amorphous solid [3], demonstrating plastic yield within a fluid shear band (or

fracture) during startup of shear flow, while a shear-dilation coupling has been shown to lead to fracture in glass-forming materials [4]. In the rubbery polymer liquid considered here, the instability is purely constitutive: Shearing leads to a decreased stress as chains are oriented along the flow direction, and the resulting fluid is mechanically unstable.

Boukany, Wang, and Wang suggested that the fracture demands new physics [5]. Certainly, current tube models are incomplete [28]. However, our calculations are reasonable if spatial features are smooth on length scales greater than the tube diameter  $a \approx 3\text{--}4$  nm. For a gap of 1 mm, the fracture width  $\delta x \approx 0.05$  corresponds to a thickness of the order of 50  $\mu\text{m}$ , which is consistent with the dimension  $\leq 40$   $\mu\text{m}$  reported in Ref. [5]. Thus, higher experimental resolution will determine whether or not the continuum nature of the tube model is adequate.

This study was funded by the EU ITN DYNACOP. We thank Robyn Moorcroft, Suzanne Fielding, and Scott Milner for helpful advice.

\*Corresponding author.

p.d.olmsted@leeds.ac.uk

- [1] M. J. Doyle, A. Maranci, E. Orowan, and S. T. Stork, *Proc. R. Soc. A* **329**, 137 (1972).
- [2] J. Lu, G. Ravichandran, and W. Johnson, *Acta Mater.* **51**, 3429 (2003).
- [3] M. L. Manning, J. S. Langer, and J. M. Carlson, *Phys. Rev. E* **76**, 056106 (2007); M. L. Manning, E. G. Daub, J. S. Langer, and J. M. Carlson, *Phys. Rev. E* **79**, 016110 (2009).
- [4] A. Furukawa and H. Tanaka, *Nat. Mater.* **8**, 601 (2009).
- [5] P. E. Boukany, S.-Q. Wang, and X. Wang, *Macromolecules* **42**, 6261 (2009).
- [6] Y. Fang, G. Wang, N. Tian, X. Wang, X. Zhu, P. Lin, G. Ma, and L. Li, *J. Rheol.* **55**, 939 (2011).
- [7] M. Doi and S. F. Edwards, *The Theory of Polymer Dynamics* (Oxford University, Oxford, 1989).
- [8] G. Marrucci and N. Grizzuti, *J. Rheol.* **27**, 433 (1983); F. A. Morrison and R. G. Larson, *J. Polym. Sci. B* **30**, 943 (1992).
- [9] J. M. Adams and P. D. Olmsted, *Phys. Rev. Lett.* **102**, 067801 (2009); J. Cao and A. E. Likhtman, *ibid.* **108**, 028302 (2012).
- [10] E. V. Menezes and W. W. Graessley, *J. Polym. Sci., Polym. Phys. Ed.* **20**, 1817 (1982).
- [11] N. A. Spenley, M. E. Cates, and T. C. B. McLeish, *Phys. Rev. Lett.* **71**, 939 (1993); P. D. Olmsted, *Rheol. Acta* **47**, 283 (2008); C.-Y. D. Lu, P. D. Olmsted, and R. C. Ball, *Phys. Rev. Lett.* **84**, 642 (2000).
- [12] T. W. Huseby, *J. Rheol.* **10**, 181 (1966); Y. H. Lin, *J. Rheol.* **29**, 605 (1985); T. C. B. McLeish and R. C. Ball, *J. Polym. Sci. B* **24**, 1735 (1986); T. C. B. McLeish, *ibid.* **25**, 2253 (1987); D. S. Malkus, J. A. Nohel, and B. J. Plohr, *SIAM J. Appl. Math.* **51**, 899 (1991); M. M. Denn, *Annu. Rev. Fluid Mech.* **22**, 13 (1990).
- [13] G. V. Vinogradov, A. Ya. Malkin, Yu. G. Yanovskii, E. K. Borisenkova, B. V. Yarlykov, and G. V. Berezhnaya, *J. Polym. Sci., A-2, Polym. Phys.* **10**, 1061 (1972).
- [14] F. J. Lim and W. R. Schowalter, *J. Rheol.* **33**, 1359 (1989); S. Q. Wang, in *Polymers in Confined Environments*, Adv. Polym. Sci. Vol. 138 (Springer, Berlin, 1999), pp. 227–275; M. M. Denn, *Annu. Rev. Fluid Mech.* **33**, 265 (2001).
- [15] G. Ianniruberto and G. Marrucci, *J. Non-Newtonian Fluid Mech.* **65**, 241 (1996); D. W. Mead and R. G. Larson, *Macromolecules* **31**, 7895 (1998).
- [16] Y. T. Hu, L. Wilen, A. Philips, and A. Lips, *J. Rheol.* **51**, 275 (2007); S. Ravindranath, S.-Q. Wang, M. Olechnowicz, and R. Quirk, *Macromolecules* **41**, 2663 (2008); P. Tapadia, S. Ravindranath, and S.-Q. Wang, *Phys. Rev. Lett.* **96**, 196001 (2006); Y. T. Hu, *J. Rheol.* **54**, 1307 (2010).
- [17] J. M. Adams and P. D. Olmsted, *Phys. Rev. Lett.* **103**, 219802 (2009); S.-Q. Wang, *ibid.* **103**, 219801 (2009).
- [18] A. E. Likhtman and R. S. Graham, *J. Non-Newtonian Fluid Mech.* **114**, 1 (2003).
- [19] R. S. Graham, A. E. Likhtman, T. C. B. McLeish, and S. T. Milner, *J. Rheol.* **47**, 1171 (2003).
- [20] P. Tapadia and S.-Q. Wang, *Phys. Rev. Lett.* **91**, 198301 (2003).
- [21] J. M. Adams, S. M. Fielding, and P. D. Olmsted, *J. Non-Newtonian Fluid Mech.* **151**, 101 (2008).
- [22] J. M. Adams, S. M. Fielding, and P. D. Olmsted, *J. Rheol.* **55**, 1007 (2011).
- [23] R. L. Moorcroft and S. M. Fielding, *Phys. Rev. Lett.* **110**, 086001 (2013).
- [24] See Supplemental Material at <http://link.aps.org/supplemental/10.1103/PhysRevLett.110.204503> for details about the stability calculation, the effects of different initial conditions, and movies.
- [25] The definition of unrelaxed segments  $\mu(t)$  matches the linear relaxation function  $G(t) \equiv \lim_{\gamma_0 \rightarrow 0} T_{x,y}(t, \gamma) / \gamma_0$ , as does the equivalent function used by Marrucci and Grizzuti for the DE model [8].
- [26] Following Ref. [8], we use the stored free energy due to the orientational distribution of tube segments, given within the independent alignment approximation by  $F(\gamma) = 1/2 \int_0^1 \ln\{1/2(1 + \gamma^2 x^2 + [(x^2 \gamma^2 - 1)^2 + 4\gamma^2 x^4]^{1/2})\} dx$ .
- [27] R. L. Moorcroft, M. E. Cates, and S. M. Fielding, *Phys. Rev. Lett.* **106**, 055502 (2011).
- [28] A. E. Likhtman, *J. Non-Newtonian Fluid Mech.* **157**, 158 (2009).

# Apparent Fracture in Polymeric Fluids under Step Shear: Supplementary Information

Okpeafoh S. Agimelen<sup>1</sup> and Peter D. Olmsted<sup>1</sup>

<sup>1</sup>*Soft Matter Physics Group, School of Physics and Astronomy,  
University of Leeds, Leeds, LS2 9JT, United Kingdom*

(Dated: April 22, 2013)

## I. CALCULATIONS

### A. Step-Strain Calculations for Different Initial Conditions

The starting point for the calculations is the diffusive Rolie-Poly (DRP) model, given by [1]

$$\frac{d\mathbf{W}}{dt} = \boldsymbol{\kappa} \cdot \mathbf{W} + \mathbf{W} \cdot \boldsymbol{\kappa}^T - \frac{1}{\tau_d}(\mathbf{W} - \mathbf{I}) - \frac{2\left(1 - \sqrt{\frac{3}{\text{Tr}\mathbf{W}}}\right)}{\tau_R} \left( \mathbf{W} + \beta \left( \frac{\text{Tr}\mathbf{W}}{3} \right)^\delta (\mathbf{W} - \mathbf{I}) \right) + \mathcal{D}\nabla^2\mathbf{W}, \quad (1)$$

where  $\mathbf{W}$  is a polymer strain,  $\kappa_{\alpha\beta} = \partial_\alpha v_\beta$ ,  $\mathbf{v}$  is the fluid velocity,  $\tau_d$  and  $\tau_R$  are the reptation and stretch relaxation times respectively,  $\mathbf{I}$  is the identity tensor,  $\beta$  measures the amount of convective constraint release in the system,  $\delta$  is a fitting parameter and  $\mathcal{D}$  is stress diffusion constant.

We use the Cartesian coordinate system (for the case of simple shear flow where the fluid is placed between two infinite parallel plates of separation  $L$ ) where  $\hat{\mathbf{y}}$  is the velocity gradient direction and  $\hat{\mathbf{x}}$  is the flow direction,  $\mathbf{v} = v_x(t, y)\hat{\mathbf{x}}$  and  $\mathbf{W} = \boldsymbol{\Delta}(t, y)$ . Substitution into Eq. 1 with  $\mathbf{W} = \boldsymbol{\Delta} + \mathbf{I}$  gives

$$\frac{\partial \Delta_{xx}}{\partial t} = 2\Delta_{xy}\hat{\gamma} - \Delta_{xx} - \frac{2\tau_d}{\tau_R}[1 - A][(\beta A + 1)\Delta_{xx} + 1] + \hat{\mathcal{D}}\frac{\partial^2 \Delta_{xx}}{\partial y^2} \quad (2a)$$

$$\frac{\partial \Delta_{xy}}{\partial t} = \hat{\gamma} + \hat{\gamma}\Delta_{yy} - \Delta_{xy} - \frac{2\tau_d}{\tau_R}[1 - A](\beta A + 1)\Delta_{xy} + \hat{\mathcal{D}}\frac{\partial^2 \Delta_{xy}}{\partial y^2} \quad (2b)$$

$$\frac{\partial \Delta_{yy}}{\partial t} = -\Delta_{yy} - \frac{2\tau_d}{\tau_R}[1 - A][(\beta A + 1)\Delta_{yy} + 1] + \hat{\mathcal{D}}\frac{\partial^2 \Delta_{yy}}{\partial y^2} \quad (2c)$$

$$A = \left( 1 + \frac{\text{Tr}\boldsymbol{\Delta}}{3} \right)^{-1/2}, \quad (2d)$$

where  $\hat{\gamma} = \dot{\gamma}\tau_d$ ,  $\hat{\mathcal{D}} = \mathcal{D}\tau_d/L^2$  [2]. The total stress  $\mathbf{T}$  is then obtained from  $\mathbf{W}$  and a Newtonian solvent of viscosity  $\eta$  as

$$\mathbf{T} = G\mathbf{W} + \eta(\boldsymbol{\kappa} + \boldsymbol{\kappa}^T) - p\mathbf{I}, \quad (3)$$

where  $G$  is the plateau modulus and  $p$  is pressure, this gives the total shear stress as

$$T_{xy} = G\Delta_{xy} + \eta\dot{\gamma}. \quad (4)$$

To capture the behaviour reported in [3], we initialize Eq. 2 with random perturbations of the form

$$\delta\mathbf{u}(0, y) = \xi \sum_{n=1}^5 (\mathbf{A}_n/n^2) \cos(n\pi y), \quad (5)$$

where  $\mathbf{u} \equiv [\hat{\gamma}, \Delta_{xx}, \Delta_{xy}, \Delta_{yy}]$ . The amplitudes  $A_{ni}$  which are the components of vector  $\mathbf{A}$  are chosen randomly within  $[-1, 1]$ . The index  $i = 1, 2, 3, 4$  corresponds to each of the quantities  $[\hat{\gamma}, \Delta_{xx}, \Delta_{xy}, \Delta_{yy}]$ . The parameter  $\xi = 0.01$  sets the overall scale of amplitude and a cosine series was chosen since it satisfies the boundary condition imposed on  $\boldsymbol{\Delta}$ . Using more modes does not change the resultant perturbation significantly due to the  $1/n^2$  penalty on the amplitudes. Each component of  $\mathbf{u}$  is initially perturbed separately using different random perturbations. Then all components of  $\mathbf{u}$  are perturbed together with each quantity receiving a separate random perturbation. Sample results from these simulations are shown in Figs. s1 to s5.

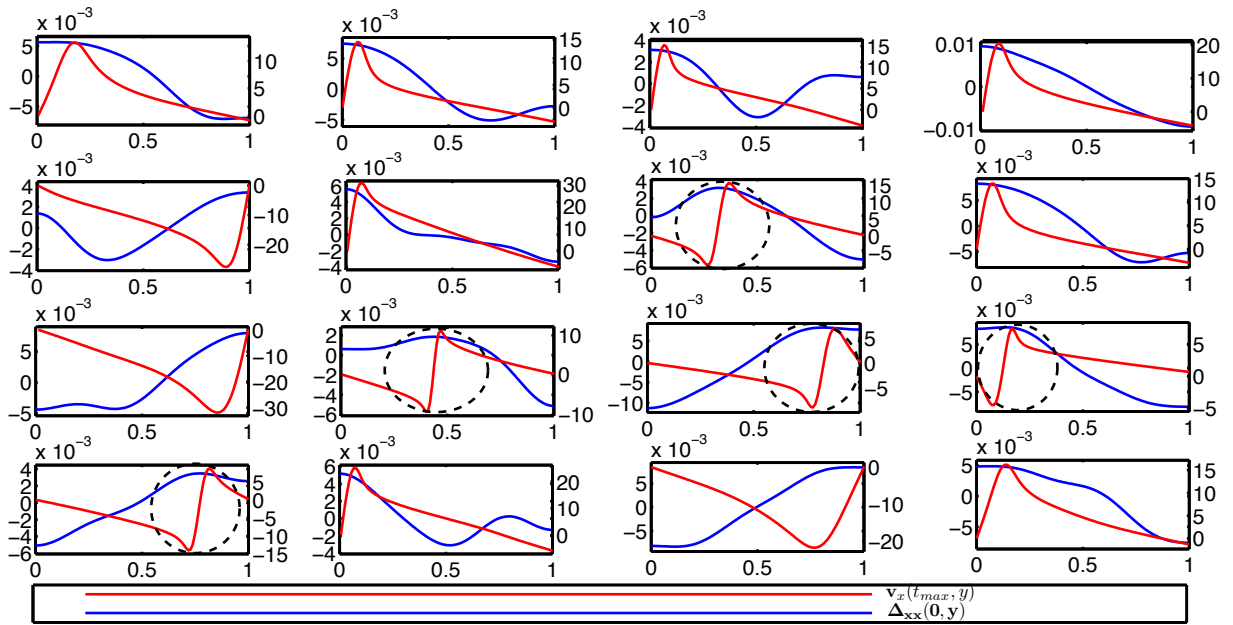


FIG. s1. Recoil or ‘fracture’ for different random initial conditions upon perturbing  $\Delta_{xx}$ . In all cases, the blue line is the perturbation and the red line is the velocity profile when both  $\mu_{\pm}$  reach their extrema together (for ‘fracture’) or  $\mu_{\pm}$  reach their extrema separately (for recoil without ‘fracture’). The ‘fracture’ profiles are indicated by the dashed circles. Left axis: perturbation; Right axis: velocity.

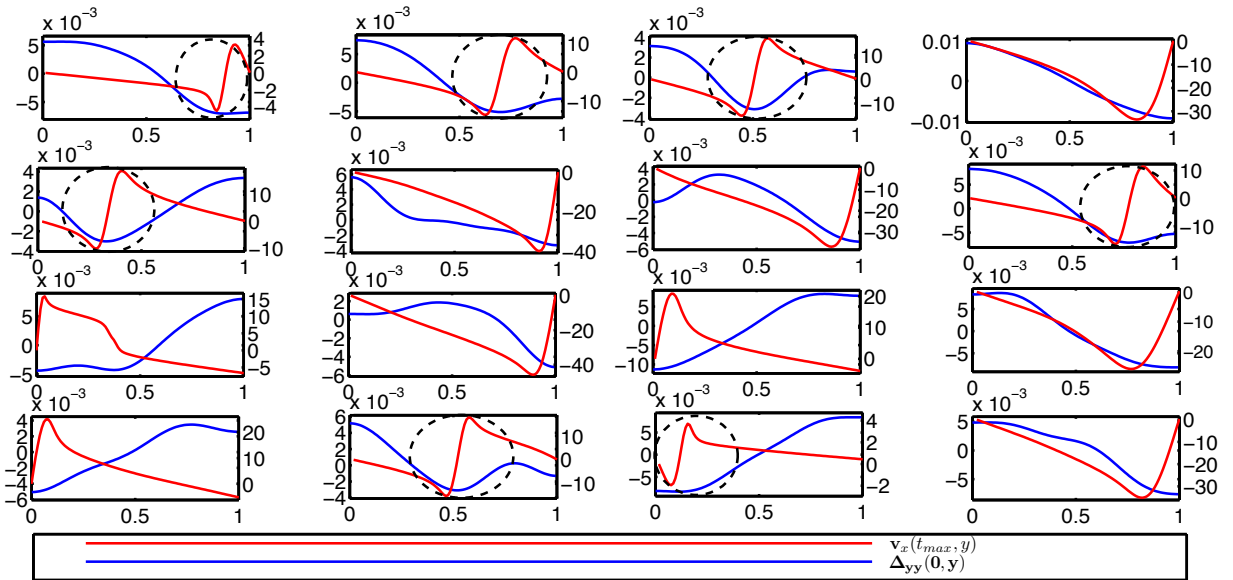


FIG. s2. Same as Figure s1 but with perturbation to  $\Delta_{yy}$ .

In all calculations reported here, the parameters were set as  $Z = \tau_d/(3\tau_R) = 72$ ,  $\widehat{D} = 10^{-5}$ ,  $\epsilon = \eta/(G\tau_d) = 10^{-4}$ ,  $\beta = 0$  and for stability analysis,  $\widehat{\rho} = 10^{-10}$ . To determine if fracture has occurred or not, consider the ‘velocity moments’  $\mu_{v_{\pm}}$ , defined by

$$\mu_{v_{\pm}} = \sum_i v_i H(\pm v_i), \quad (6)$$

where the sum is over all spatial positions  $y_i$  and  $H$  is the Heaviside step function. If both positive moment  $\mu_{v_+}$

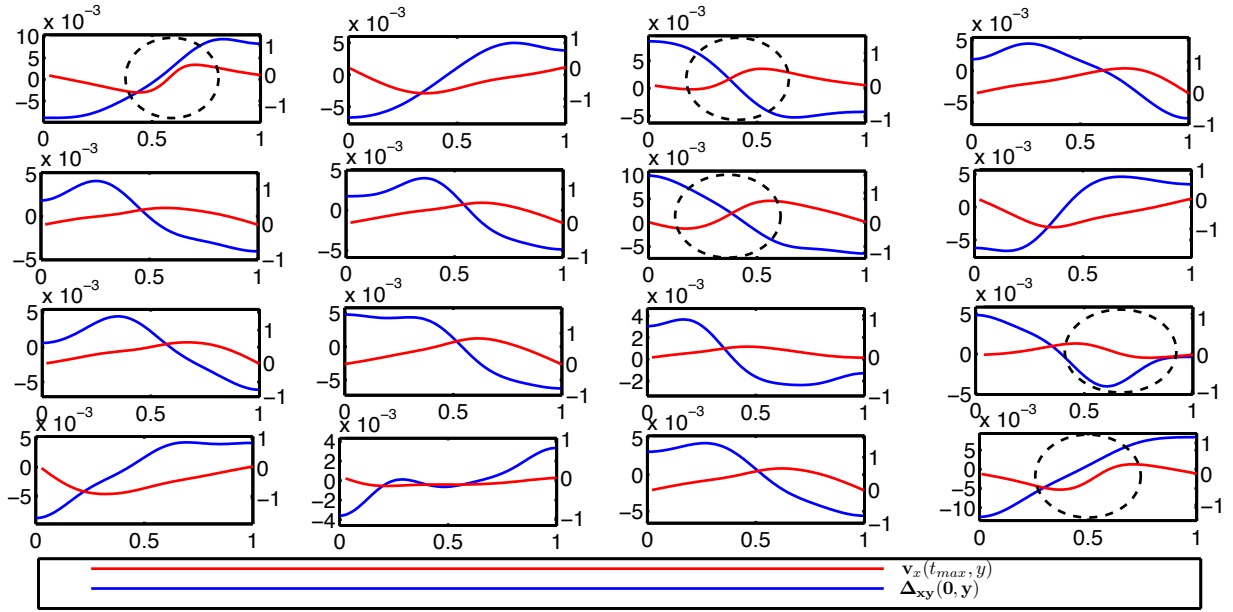


FIG. s3. Perturbation of  $\Delta_{xy}$ . Only a weak recoil or a weak sign of ‘fracture’ is seen in this case. The blue and red lines have the same meaning as in Fig. s1. The ‘weak fracture’ profiles are indicated by the dashed circles. Left axis: perturbation; Right axis: velocity.

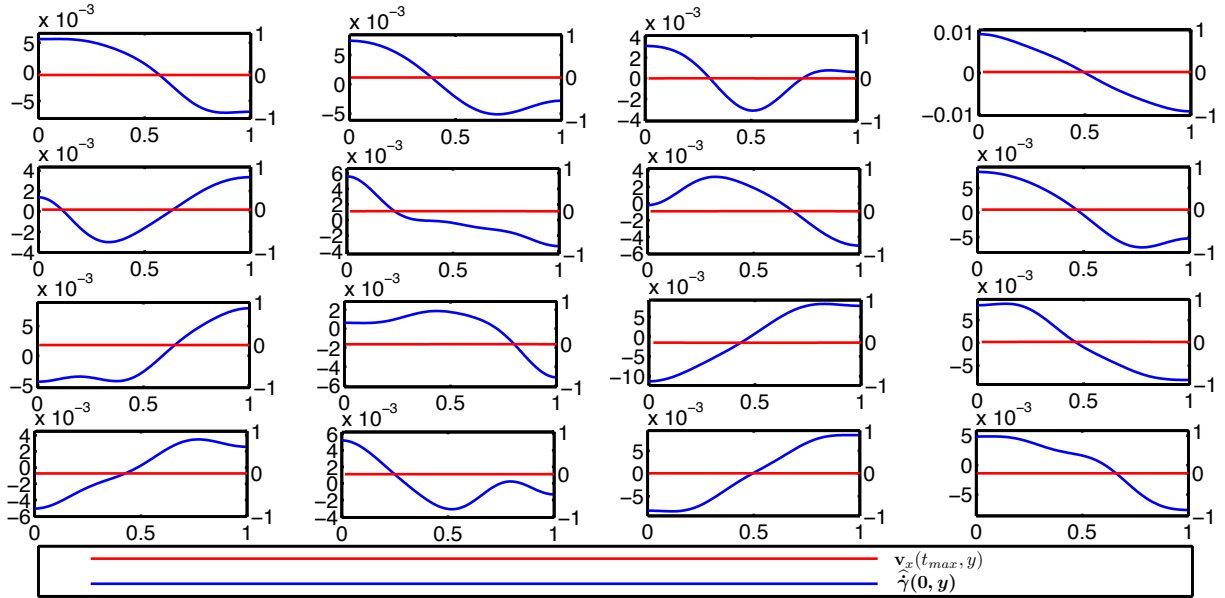


FIG. s4. Same as Figure s3 but with perturbation to  $\hat{\gamma}$ .

and negative moment  $\mu_{v-}$  occur together at any time during stress relaxation after shear cessation, then we say that ‘fracture’ has occurred, otherwise there is no fracture. The velocity profiles shown in Figs. s1 to s5 occur at the time when both  $\mu_{v+}$  and  $\mu_{v-}$  reach their extrema for the case of fracture. When there is no fracture, the velocity profiles are shown when either  $\mu_{v+}$  reaches its maximum or  $\mu_{v-}$  reaches its minimum. When fracture occurs, the position of the fracture plane depends on the shape of the specific perturbation. The stress relaxation is independent of the position of the fracture plane, as in the experiments of [3] (section III A).

In about 34% of 300 simulations where  $\Delta_{xx}$ ,  $\Delta_{yy}$ ,  $\Delta_{xy}$  and  $\hat{\gamma}$  are all perturbed simultaneously, the resultant velocity profiles resemble the type reported in [3]. The calculations in the manuscript use a set of initial conditions that give

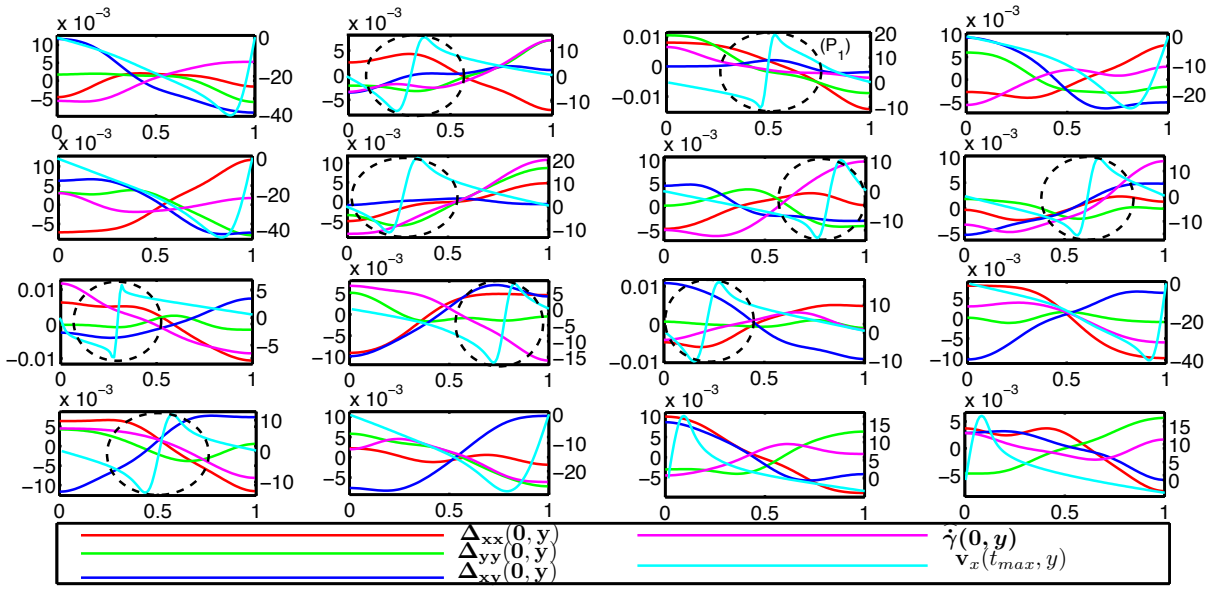


FIG. s5. Recoil or ‘fracture’ upon perturbing all components, with each component receiving a separate random perturbation. Red line: perturbation to  $\Delta_{xx}$ . Green line: perturbation to  $\Delta_{yy}$ . Blue line: perturbation to  $\Delta_{xy}$ . Magenta line: perturbation to  $\dot{\gamma}$ . Cyan line: recoil or ‘fracture’ velocity profile  $v$ . Left axis: perturbation; Right axis: velocity. In all cases, the ‘fracture’ profiles are indicated with the dashed circles.

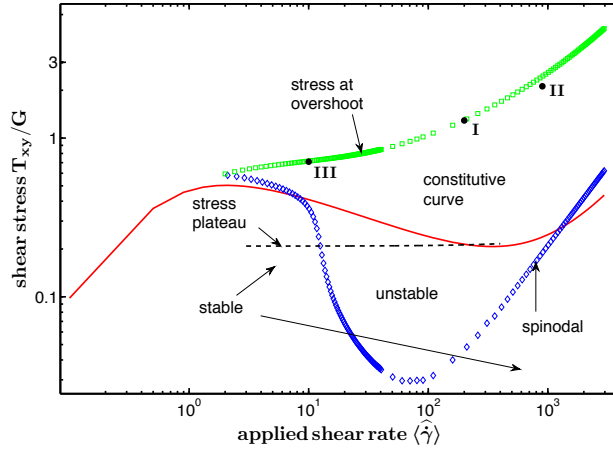


FIG. s6. Spinodal (shear stresses at which the perturbation imposed on the base state at  $t_0$  grow), constitutive curve, stress plateau and the overshoot stress for the DRP model. The stresses at shear cessation for the three Cases discussed in the manuscript are indicated as I, II and III. Parameters:  $\beta = 0$ ,  $Z = \tau_d / (3\tau_R) = 72$ .

a fracture with all quantities perturbed, such as subfigure  $P_1$  in Fig. s5.

### B. Linear stability analysis

Linear stability analysis is carried out by considering the stability of a homogeneous base state  $\mathbf{s}(t)$  to fluctuations. During the evolution of the base state  $\mathbf{s}(t)$ , a perturbation  $\delta\mathbf{u}(t, y) = [\delta\Delta_{xx}, \delta\Delta_{xy}, \delta\Delta_{yy}, \delta\hat{\gamma}](t, y)$  is introduced at some time  $t_0$ . Subsequent evolution of the perturbation is then given by

$$\mathbf{u}(t - t_0, y) = [\hat{\gamma}, \mathbf{s}](t_0) + \delta\mathbf{u}(t - t_0, y). \quad (7)$$

If the perturbation grows at early times after shear cessation at  $t_0$ , then it may be able to induce ‘fracture’ at later times. The homogeneous base state  $\mathbf{s}(t) = [\widehat{\gamma}, \overline{\Delta}_{xx}, \overline{\Delta}_{xy}, \overline{\Delta}_{yy}]$  is obtained by solving

$$\partial_t \overline{\Delta}_{xx} = 2\overline{\Delta}_{xy} \widehat{\gamma} - \overline{\Delta}_{xx} - \frac{2\tau_d}{\tau_R} [1 - \overline{A}] [(\beta\overline{A} + 1) \overline{\Delta}_{xx} + 1] \quad (8a)$$

$$\partial_t \overline{\Delta}_{xy} = \widehat{\gamma} + \widehat{\gamma} \overline{\Delta}_{yy} - \overline{\Delta}_{xy} - \frac{2\tau_d}{\tau_R} [1 - \overline{A}] (\beta\overline{A} + 1) \overline{\Delta}_{xy} \quad (8b)$$

$$\partial_t \overline{\Delta}_{yy} = -\overline{\Delta}_{yy} - \frac{2\tau_d}{\tau_R} [1 - \overline{A}] [(\beta\overline{A} + 1) \overline{\Delta}_{yy} + 1] \quad (8c)$$

$$\overline{A} = \left( 1 + \frac{\text{Tr} \overline{\mathbf{\Delta}}}{3} \right)^{-1/2}. \quad (8d)$$

The perturbation  $\delta \mathbf{u}(t, y)$  consists of fluctuations in the velocity gradient direction of the form

$$\delta \mathbf{u}(t, y) = \sum_k \delta \mathbf{u}_k(t) \exp(iky) \quad t \geq t_0. \quad (9)$$

Substituting Eq. 7 into Eq. 2 and the momentum equation

$$\rho \frac{d\mathbf{v}}{dt} \equiv \rho \left[ \frac{\partial}{\partial t} + (\mathbf{v} \cdot \nabla) \right] \mathbf{v} = \nabla \cdot \mathbf{T}, \quad (10)$$

where  $\rho$  is the fluid density, gives

$$\begin{aligned} \partial_t \delta \Delta_{xx,k}(t) &= \left[ \frac{\tau_d}{3\tau_R} \overline{\Delta}_{xx} (\beta - 1) \overline{A}^3 - 1 - \frac{\tau_d}{3\tau_R} \overline{A}^3 - 2 \frac{\tau_d}{\tau_R} [1 + (\beta - 1) \overline{A}] - \frac{2}{3} \beta \overline{\Delta}_{xx} \overline{A}^4 + 2\beta \overline{A}^2 \right. \\ &\quad \left. - k^2 \widehat{\mathcal{D}} \right] \delta \Delta_{xx,k}(t) \\ &\quad + 2\widehat{\gamma} \delta \Delta_{xy,k}(t) \\ &\quad + \left[ (\beta - 1) \frac{\tau_d}{3\tau_R} \overline{\Delta}_{xx} \overline{A}^3 - \frac{\tau_d}{3\tau_R} \overline{A}^3 - \frac{2}{3} \beta \overline{\Delta}_{xx} \overline{A}^4 \right] \delta \Delta_{yy,k}(t) \\ &\quad + 2\overline{\Delta}_{xy} \delta \widehat{\gamma}_k(t) \end{aligned} \quad (11a)$$

$$\begin{aligned} \partial_t \delta \Delta_{xy,k}(t) &= \left[ (\beta - 1) \frac{\tau_d}{3\tau_R} \overline{\Delta}_{xy} \overline{A}^3 - \frac{2}{3} \beta \frac{\tau_d}{\tau_R} \overline{A}^4 \overline{\Delta}_{xy} \right] \delta \Delta_{xx,k}(t) \\ &\quad + \left[ 2\beta \frac{\tau_d}{\tau_R} \overline{A}^2 - 1 - 2 \frac{\tau_d}{\tau_R} [1 + (\beta - 1) \overline{A}] - k^2 \widehat{\mathcal{D}} \right] \delta \Delta_{xy,k}(t) \\ &\quad + \left[ \widehat{\gamma} + (\beta - 1) \frac{\tau_d}{3\tau_R} \overline{\Delta}_{xy} \overline{A}^3 - \frac{2}{3} \beta \frac{\tau_d}{\tau_R} \overline{\Delta}_{xy} \overline{A}^4 \right] \delta \Delta_{yy,k}(t) \\ &\quad + [1 + \overline{\Delta}_{yy}] \delta \widehat{\gamma}_k(t) \end{aligned} \quad (11b)$$

$$\begin{aligned} \partial_t \delta \Delta_{yy,k}(t) &= \left[ (\beta - 1) \frac{\tau_d}{3\tau_R} \overline{\Delta}_{yy} \overline{A}^3 - \frac{\tau_d}{3\tau_R} \overline{A}^3 - \frac{2}{3} \beta \frac{\tau_d}{\tau_R} \overline{\Delta}_{yy} \overline{A}^4 \right] \delta \Delta_{xx,k}(t) \\ &\quad + \left[ \frac{\tau_d}{3\tau_R} (\beta - 1) \overline{\Delta}_{yy} \overline{A}^3 - 1 - \frac{\tau_d}{3\tau_R} \overline{A}^3 - 2 \frac{\tau_d}{\tau_R} [1 + (\beta - 1) \overline{A}] - \frac{2}{3} \beta \frac{\tau_d}{\tau_R} \overline{\Delta}_{yy} \overline{A}^4 \right. \\ &\quad \left. + 2\beta \frac{\tau_d}{\tau_R} \overline{A}^2 - k^2 \widehat{\mathcal{D}} \right] \delta \Delta_{yy,k}(t) \end{aligned} \quad (11c)$$

$$\partial_t \delta \widehat{\gamma}_k(t) = -\frac{k^2}{\widehat{\rho}} \delta \Delta_{xy,k}(t) - \frac{k^2 \epsilon}{\widehat{\rho}} \delta \widehat{\gamma}_k(t) \quad (11d)$$

$$\epsilon = \frac{\eta}{G\tau_d} \quad (11e)$$

$$\widehat{\rho} = \frac{\rho L^2}{G\tau_d^2}, \quad (11f)$$

where all nonlinear terms in  $[\delta\Delta_{xx,k}, \delta\Delta_{xy,k}, \delta\Delta_{yy,k}, \delta\hat{\gamma}_k]$  have been neglected. In the zero Reynolds number limit  $\hat{\rho} \rightarrow 0$  this reduces to

$$\begin{aligned} \partial_t \delta\Delta_{xx,k}(t) = & \left[ \frac{\tau_d}{3\tau_R} \bar{\Delta}_{xx} (\beta - 1) \bar{A}^3 - 1 - \frac{\tau_d}{3\tau_R} \bar{A}^3 - 2 \frac{\tau_d}{\tau_R} [1 + (\beta - 1) \bar{A}] - \frac{2}{3} \beta \bar{\Delta}_{xx} \bar{A}^4 + 2\beta \bar{A}^2 \right. \\ & \left. - k^2 \hat{\mathcal{D}} \right] \delta\Delta_{xx,k}(t) \\ & + 2 \left[ \hat{\gamma} - \frac{\bar{\Delta}_{xy}}{\epsilon} \right] \delta\Delta_{xy,k}(t) \\ & + \left[ (\beta - 1) \frac{\tau_d}{3\tau_R} \bar{\Delta}_{xx} \bar{A}^3 - \frac{\tau_d}{3\tau_R} \bar{A}^3 - \frac{2}{3} \beta \bar{\Delta}_{xx} \bar{A}^4 \right] \delta\Delta_{yy,k}(t) \end{aligned} \quad (12a)$$

$$\begin{aligned} \partial_t \delta\Delta_{xy,k}(t) = & \left[ (\beta - 1) \frac{\tau_d}{3\tau_R} \bar{\Delta}_{xy} \bar{A}^3 - \frac{2}{3} \beta \frac{\tau_d}{\tau_R} \bar{A}^4 \bar{\Delta}_{xy} \right] \delta\Delta_{xx,k}(t) \\ & + \left[ 2\beta \frac{\tau_d}{\tau_R} \bar{A}^2 - 1 - 2 \frac{\tau_d}{\tau_R} [1 + (\beta - 1) \bar{A}] - \frac{1 + \bar{\Delta}_{yy}}{\epsilon} - k^2 \hat{\mathcal{D}} \right] \delta\Delta_{xy,k}(t) \\ & + \left[ \hat{\gamma} + (\beta - 1) \frac{\tau_d}{3\tau_R} \bar{\Delta}_{xy} \bar{A}^3 - \frac{2}{3} \beta \frac{\tau_d}{\tau_R} \bar{\Delta}_{xy} \bar{A}^4 \right] \delta\Delta_{yy,k}(t) \end{aligned} \quad (12b)$$

$$\begin{aligned} \partial_t \delta\Delta_{yy,k}(t) = & \left[ (\beta - 1) \frac{\tau_d}{3\tau_R} \bar{\Delta}_{yy} \bar{A}^3 - \frac{\tau_d}{3\tau_R} \bar{A}^3 - \frac{2}{3} \beta \frac{\tau_d}{\tau_R} \bar{\Delta}_{yy} \bar{A}^4 \right] \delta\Delta_{xx,k}(t) \\ & + \left[ \frac{\tau_d}{3\tau_R} (\beta - 1) \bar{\Delta}_{yy} \bar{A}^3 - 1 - \frac{\tau_d}{3\tau_R} \bar{A}^3 - 2 \frac{\tau_d}{\tau_R} [1 + (\beta - 1) \bar{A}] - \frac{2}{3} \beta \frac{\tau_d}{\tau_R} \bar{\Delta}_{yy} \bar{A}^4 \right. \\ & \left. + 2\beta \frac{\tau_d}{\tau_R} \bar{A}^2 - k^2 \hat{\mathcal{D}} \right] \delta\Delta_{yy,k}(t) \end{aligned} \quad (12c)$$

This is a matrix equation of the form

$$\partial_t \delta \tilde{\mathbf{u}}(t) = \mathbf{M}(t_0) \cdot \delta \tilde{\mathbf{u}}(t) \quad t \geq t_0, \quad (13)$$

where  $\tilde{\mathbf{u}} = [\Delta_{xx}, \Delta_{xy}, \Delta_{yy}]$ . Similar to the case described in [4], the eigenvalues of the stability matrix  $\mathbf{M}(t_0)$  determine the (in)stability of the system. We infer instability when the the largest real part of an eigenvalue just becomes positive [4]. In this situation the perturbations grow exponentially. Hence the spinodal (the shear stress at which the fluid goes unstable during startup) for the system can be constructed as shown in Fig. s6. This region of instability matches the constitutive curve, similar to the situation reported in [4].

When the perturbation given in Eq. 5 is used to initialize the system, it induces some inhomogeneity in the system. Each point in space can then be considered as a base state and the stability of each of these base states to small amplitude fluctuations is also described by the stability matrix  $\mathbf{M}(t_0)$ . Hence the most unstable of these base states (which is the state whose eigenvalue has the largest real part) can be determined. This approach gives insight into the behaviour of the system when the quantities  $\hat{\gamma}$ ,  $\Delta_{xx}$ ,  $\Delta_{xy}$  and  $\Delta_{yy}$  are perturbed separately. For 15 different initial conditions that give a ‘fracture’ profile, the eigenvector  $\tilde{\mathbf{v}}_m$  corresponding to the maximum real eigenvalue in space at the time of stretch relaxation is heavily dominated by the components  $\Delta_{xx}$  and  $\Delta_{yy}$ . The components of  $\tilde{\mathbf{v}}_m$  for these different initial conditions are shown in Table I, where  $\tilde{v}_m^{xx}$  is the component in the flow direction,  $\tilde{v}_m^{xy}$  is the component in the shear direction and  $\tilde{v}_m^{yy}$  is the component in the velocity gradient direction. Hence perturbing the components  $\hat{\gamma}$  and  $\Delta_{xy}$  separately do not induce ‘fracture’ (as in Figs. s3 and s4) as compared with perturbing the components  $\Delta_{xx}$  and  $\Delta_{yy}$  separately at the same amplitude (as in Figs. s1 and s2).

### C. Comparison with experiment

The calculations in the manuscript are based on the sample SBR 250K whose rheological properties are reported in Tables 1 and 2 of [3]. The rheological properties reported in Table 2 of [3] were said to have been measured from linear viscoelastic measurements (see section II B of [3]) but the Rouse times reported in Table 2 were estimated using  $\tau_R^w = \tau_d/(M_w/M_e)$ , where  $\tau_d$  is the reptation time (section II B of [3]). However, in our manuscript the Rouse time is calculated using  $\tau_R = \tau_d/(3Z)$  (as given in section I of [5]), where  $Z = M_w/M_e$  is the number of entanglements per chain. This then implies that the values of  $\tau_R^w$  quoted in Table 2 of [3] are larger than the values of  $\tau_R$  used in our manuscript by a factor of 3. We then present the data in [3] as different cases.

TABLE I. Components of most unstable eigenvector  $\tilde{\mathbf{v}}_m$  for 15 different initial conditions, for  $\langle \dot{\gamma} \rangle = 200$ ,  $\gamma_0 = 2.5$ .

Initial Condition	$\tilde{v}_m^{xx}$	$\tilde{v}_m^{xy}$	$\tilde{v}_m^{yy}$
1	0.9657	-0.0115	-0.2594
2	0.9767	-0.0131	-0.2144
3	0.9678	-0.0118	-0.2516
4	0.9730	-0.0125	-0.2304
5	0.9632	-0.0112	-0.2687
6	0.9667	-0.0117	-0.2555
7	0.9678	-0.0118	-0.2513
8	0.9636	-0.0113	-0.2672
9	0.9739	-0.0127	-0.2266
10	0.9683	-0.0119	-0.2496
11	0.9675	-0.0118	-0.2524
12	0.9742	-0.0127	-0.2255
13	0.9666	-0.0116	-0.2562
14	0.9613	-0.0110	-0.2753
15	0.9596	-0.0109	-0.2812

**Case I: Intermediate Shear Rate, High Strain**– Using  $\langle \dot{\gamma} \rangle = 0.7 \text{ s}^{-1}$  given in Fig. 1a of [3] and  $\tau_R^w = 4.1 \text{ s}$  quoted in Table 2 of [3] (for the sample SBR 250K) gives  $\langle \dot{\gamma} \rangle \tau_R^w \simeq 2.9$ . The sample SBR 250K (see Table 2 of [3]) has  $M_w = 250000 \text{ g/mol}$  and  $M_e = 3300 \text{ g/mol}$ , which gives  $Z = 76$ . Then using  $Z = 76$ ,  $\langle \dot{\gamma} \rangle \tau_d = 200$  and  $\tau_d/\tau_R = 3Z$  gives  $\langle \dot{\gamma} \rangle \tau_R \simeq 0.95$ , which is comparable to the value of  $\langle \dot{\gamma} \rangle \tau_R \simeq 1$  specified in case I of the manuscript, this is consistent with Fig. 1 of [3].

**Case II: High Shear Rate, Low Strain**– Similarly,  $\langle \dot{\gamma} \rangle = 14 \text{ s}^{-1}$  from [3] gives  $\langle \dot{\gamma} \rangle \tau_R^w \simeq 57$ , which is consistent with  $\langle \dot{\gamma} \rangle \tau_R > 1$  given in case II of the manuscript and it agrees with Fig. 2 of [3].

**Case III: Low Shear Rate, Low Strain**– Again,  $\langle \dot{\gamma} \rangle = 0.05 \text{ s}^{-1}$  gives  $\langle \dot{\gamma} \rangle \tau_R^w \simeq 0.2$ , which is consistent with  $\langle \dot{\gamma} \rangle \tau_R < 1$  given in case III of the manuscript, this has close agreement with Fig. 7 of [3].

The shear stresses at the time of shear cessation for the three cases I, II and III are indicated in Fig. s6. In case I, the shear stress had gone through the overshoot and it is beginning to decrease. In case two, the flow is switched off before the shear stress reaches the overshoot. Finally, in case III the flow is switched off just before the shear stress reaches the overshoot. Figure 1(c) of the manuscript shows a comparison of velocity profiles from the simulations and experimental data; the experimental data were obtained from  $V_{max}$  in Fig. 1c of [3], made dimensionless using  $\hat{V}_{max} = V_{max}\tau/L$ , where  $\tau = 310 \text{ s}$  (from Table 2 of [3]) and  $L = 0.7 \text{ mm}$  as given in section II of [3].

**Induction time**–To check the variation of the delay time after shear cessation before fracture sets in, we performed calculations at three different shear rates satisfying  $\langle \dot{\gamma} \rangle \tau_R > 1$  (with  $\tau_R$  fixed), similar to Fig. 6 of [3]. For  $\langle \dot{\gamma} \rangle = 600$ ,  $\langle \dot{\gamma} \rangle \tau_R \simeq 2.8$ ,  $\langle \dot{\gamma} \rangle = 800$ ,  $\langle \dot{\gamma} \rangle \tau_R \simeq 3.7$  and  $\langle \dot{\gamma} \rangle = 1000$ ,  $\langle \dot{\gamma} \rangle \tau_R \simeq 4.6$ . In all cases, the applied strains indicated by the lines  $l_1$  and  $l_2$  in Fig. s7(a), are below the strain for overshoot at the applied shear rate. The overshoot stress is a linear function of the overshoot strain, as in Fig. 6(a) of [3]. Figures s7(bcd) show that, for varying strain and given shear rate, the higher plateau stress after stretch relaxation leads to a longer induction time. This characteristic is similar to the the situation in the inset of Fig. 6(b) of [3].

Figures. s7(e-f) show that for fixed strain and varying shear rate, the plateau stresses collapse, and the lower applied shear rate leads to a slightly longer induction time for  $\gamma_0 = 2.2$ . This can be linked to the faster growth rate  $\omega_{max}$  observed for the very high shear rates, in which the viscous contribution to the instability dominates. However, this behaviour does *not* match that displayed in the inset of Fig. 6(b) of [3], in which the *higher* applied shear rate resulted in a larger induction time. We do not have an adequate explanation for these discrepancies.

## II. MOVIES

The movies in <https://eudoxus.leeds.ac.uk/dynacop/FracturePage.html> illustrate the cases where the fluid undergoes fracture after shear cessation (**Fracture.avi**) and recoil without fracture (**Recoil.avi**) for case I. To achieve this, an initial condition of the form  $\Delta_{xx}(0, y) = A(\cos(\pi y) + \phi \cos(2\pi y))$  is used to perturb the system. The

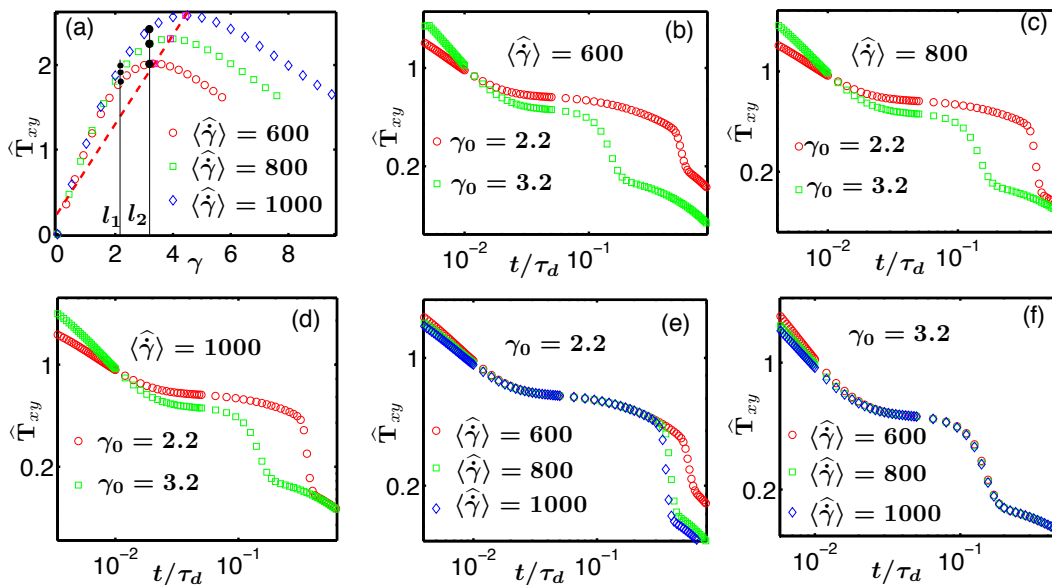


FIG. s7. (a) Shear stress versus strain at the three different applied shear rates indicated in the figure such that  $\langle \hat{\gamma} \rangle_{\tau_R} > 1$  in all cases, red circles:  $\langle \hat{\gamma} \rangle_{\tau_R} = 2.8$ , green squares:  $\langle \hat{\gamma} \rangle_{\tau_R} = 3.7$  and blue diamonds:  $\langle \hat{\gamma} \rangle_{\tau_R} = 4.6$ . The dashed line connects the strains for overshoot and their corresponding stresses for each applied shear rate, while the lines  $l_1$  and  $l_2$  indicate the applied strains  $\gamma_0 = 2.2$  and  $\gamma_0 = 3.2$  respectively. (b)-(f) Stress relaxation after step strains at different applied strains  $\gamma_0$  and shear rates  $\langle \hat{\gamma} \rangle$  indicated. Parameters as in Fig. s4.

shape and amplitude of this perturbation can be tuned to bring it close to one of the random perturbations which yields fracture-like behaviour when the component  $\Delta_{xx}$  is perturbed. The amplitude is fixed at  $A = 0.006$  while the parameter  $\phi$  is varied to change the shape of the perturbation. The shapes of this perturbation for  $\phi = 0.25$  and  $\phi = 0.67$  are shown in Fig. s8(a).

For  $\phi = 0.67$ , the fluid fractures after shear cessation, the window on the left of `Fracture.avi` shows the fluid velocity from startup (with the upper plate fixed and the lower plate moving) to shear cessation and continues until the end of fracture. Before shear cessation, the fluid is seen to be moving to the left, after which the flow is switched off and the velocity vectors go to zero momentarily (except with a slight bulge due to the initial perturbation). The sizes of the velocity vectors before shear cessation are larger than their sizes after shear cessation by roughly one order of magnitude, hence to make the figure visible in the video, a rescaling of the figure window was carried out after shear cessation. The velocity profile  $v$  in the video on the left was made dimensionless using  $\hat{v} = v\tau_d/L$ . Then using  $\tau_d = 310$  s and  $L = 0.7$  mm (from [3]) gives the maximum size of velocity vectors  $v_{max}$  before shear cessation roughly equal to  $0.45$  mm s $^{-1}$  and the maximum size after shear cessation is roughly equal to  $0.02$  mm s $^{-1}$ . The velocity profile during fracture is shown in Fig. s8(b).

The figure window on the right of `Fracture.avi` shows the corresponding total shear stress  $T_{xy}/G$  from startup until the end of fracture. The total shear stress builds up quickly when the flow is switched on, and then just after the overshoot when the flow is switched off, the total shear stress goes through an initial quick relaxation during which the polymer chains relax stretch. It then enters a slow relaxation when reptation sets in. Although some reptation had already occurred during stretch relaxation, it becomes the dominant mechanism for stress relaxation after stretch relaxation. However, before reptation can completely relax the stress, the growing perturbation causes a sudden quick relaxation of stress. By this time the ‘fracture plane’ is fully developed and the fluid can be seen moving rapidly in two different directions on both sides of this plane. Finally when this rapid motion ceases, the stress resumes its slow relaxation and the material appears to have healed itself.

The case of  $\phi = 0.25$ , where there is no peak in the initial perturbation as in Fig. s8(a), gives a completely different relaxation behaviour in the fluid as shown in `Recoil.avi`. The left window of that figure shows the fluid velocity from startup to shear cessation and beyond. Like in the case of  $\phi = 0.67$ , the top plate is fixed while the lower plate moves to the left. After shear cessation, the perturbation is seen to grow for a while but the fluid does not ‘break’ in two unlike in the case of  $\phi = 0.67$ . The growing perturbation loses the competition against the background reptation and hence the material heals itself and the fluid velocity vanishes after some time. Like in the case of  $\phi = 0.67$ , the figure window has been rescaled after shear cessation to make the velocity vectors visible. The maximum size of the

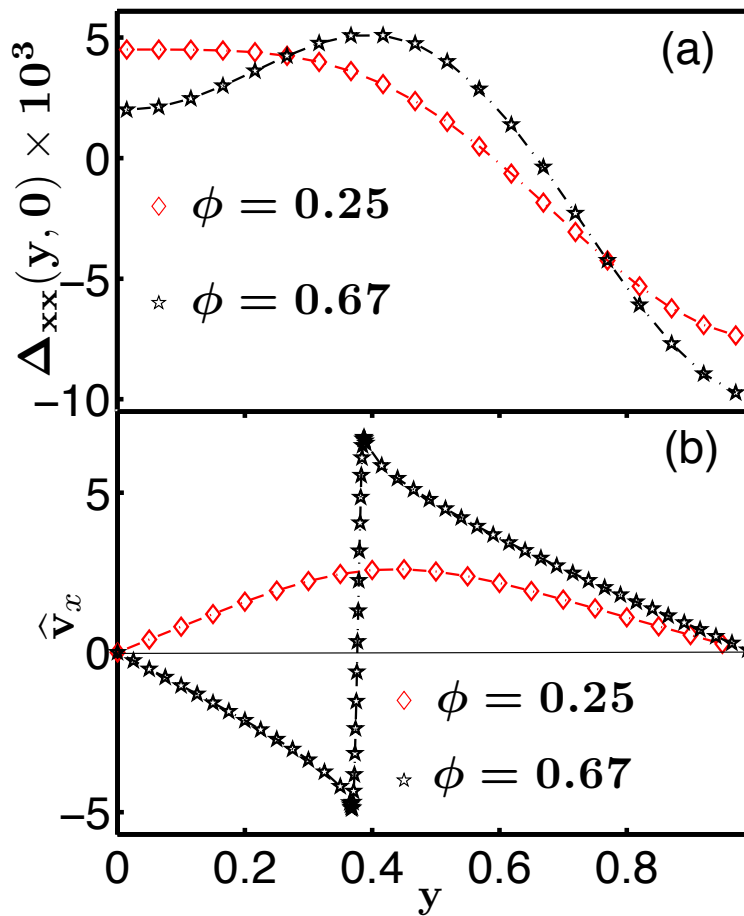


FIG. s8. (a) Initial perturbation for:  $\phi = 0.25$  and  $\phi = 0.67$ , as shown in the movies `Recoil.avi` and `Fracture.avi`. (b) Recoil after shear cessation for  $\phi = 0.25$  and fracture after shear cessation for  $\phi = 0.67$ . Parameters:  $\beta = 0$ ,  $Z = \tau_d/(3\tau_R) = 72$ ,  $\langle \hat{\gamma} \rangle = 200$ , and  $\gamma_0 = 2.5$ .

velocity vectors before shear cessation is roughly equal to  $0.45 \text{ mm s}^{-1}$  while the maximum size after shear cessation is roughly equal to  $0.006 \text{ mm s}^{-1}$ . The recoil velocity for this case is shown in Fig. s8(b).

The right window of `Recoil.avi` shows the corresponding time dependent total shear stress for this case. It grows quickly from startup like the case of  $\phi = 0.67$ , then decays quickly during stretch relaxation and ends up with a slow relaxation due to reptation. The stress does not show any stage of rapid relaxation again since reptation is the dominant mechanism for stress relaxation in this case.

The movies were made with a mesh of 100 grid points to reduce the computational time. The relevant parameters were  $Z = 72$ ,  $\hat{D} = 10^{-5}$ ,  $\epsilon = 10^{-4}$ ,  $\beta = 0$ ,  $\gamma_0 = 2.5$  and  $\langle \hat{\gamma} \rangle = 200$ , which represent case I described in the manuscript.

- 
- [1] A. E. Likhtman and R. S. Graham, *J. Non-Newton. Fl. Mech.* **114**, 1 (2003); J. M. Adams and P. D. Olmsted, *Phys. Rev. Lett.* **102**, 067801 (2009).
  - [2] The time  $t$  and spatial variables  $y$  have been made dimensionless as  $\hat{t} = t/\tau_d$  and  $\hat{y} = y/L$  respectively. However, for simplicity the quantities  $\hat{t}$  and  $\hat{y}$  have been written as  $t$  and  $y$  in Eq. 2.
  - [3] P. E. Boukany, S.-Q. Wang, and X. Wang, *Macromolecules* **42**, 6261 (2009).
  - [4] S. M. Fielding and P. D. Olmsted, *Phys. Rev. Lett.* **90**, 224501 (2003).
  - [5] R. S. Graham, A. E. Likhtman, T. C. B. McLeish, and S. T. Milner, *J. Rheol.* **47**, 1171 (2003).